Toward Practical HARQ-Based RC-LDPC Design for Optical Satellite-Assisted Vehicular Networks

Cuong T. Nguyen, *Student Member, IEEE,* Hoang D. Le, *Member, IEEE,* Chuyen T. Nguyen, and Anh T. Pham, *Senior Member, IEEE*

Abstract

Free-space optics (FSO)-based low-Earth orbit (LEO) satellite systems have recently aroused considerable attention as an enabling technology for the Internet of Vehicles (IoVs) applications. However, such systems face critical challenges, including cloud coverage, atmospheric turbulence, and pointing errors. This paper addresses a link-layer error-control design solution, which is a combination of the low-density parity check (LDPC) code and the incremental redundancy (IR)-hybrid automatic repeat request (HARQ) protocol. We consider a subclass of rate-compatible (RC)-LDPC code extension, i.e., protograph-based raptor-like (PBRL)-LDPC codes, for the proposed IR-HARQ design. In addition, we provide a comprehensive analytical framework to obtain performance metrics, including goodput, energy efficiency, and average frame delay. Numerical results highlight the outperformance of the design proposal compared to conventional link-layer solutions in FSO-based LEO satellite systems. Also, we provide a design guideline regarding the proper selection of transmitted power and decoding complexity concerns. Furthermore, we investigate the feasibility of our design proposal for a study case involving the existing Japan LEO satellite networks and the moving vehicles. Finally, we conduct the Monte-Carlo simulations to validate the correctness of theoretical results.

Index Terms

Cuong T. Nguyen, Hoang D. Le, and Anh T. Pham are with the School of Computer Science and Engineering, The University of Aizu, Aizuwakamatsu 965-8580, Japan (email: cuong98hp@gmail.com; hoangle@u-aizu.ac.jp; pham@u-aizu.ac.jp).

Chuyen T. Nguyen is with Hanoi University of Science and Technology, Vietnam (email: chuyen.nguyenthanh@hust.edu.vn).

Corresponding author: Hoang D. Le.

Free-space optics (FSO), hybrid automatic repeat request (HARQ), protograph-based raptor-like LDPC code (PBRL-LDPC), low earth orbits (LEO) satellite.

I. INTRODUCTION

Recent years have witnessed the rapid development of the Internet of Vehicles (IoV) for many emerging applications, e.g., high-speed Internet for vehicles, autonomous cars, and vehicle-aided post-disaster communication [1]. The growing capacity demand and ubiquitous coverage requirement of IoV pose various challenges for traditional terrestrial networks using radio-frequency (RF) communications. On the other hand, low-Earth orbit (LEO) satellites have aroused considerable attention in many ambitious projects of Amazon's Kuiper, SpaceX's Starlink, and Telesat, thanks to global coverage capability and low latency/power consumption (compared to other satellite types) [2]. In addition, free-space optical (FSO) communication is renowned for its exceptional high-speed connectivities facilitated by a vast license-free optical bandwidth [3]. As a result, FSO-based LEO satellite systems emerge as a pivotal enabling technology for future IoV networks [4]. Nevertheless, major degrading factors on FSO-based LEO satellite links are the Doppler effect, cloud coverage, transceiver misalignment, and atmospheric turbulence [5]. These adverse issues significantly deteriorate the performance of such systems, requiring extensive research endeavors to address.

A. Related Works

To ensure reliable data transmissions, hybrid automatic repeat request (HARQ) is a viable error-control solution. The HARQ schemes, combining automatic repeat requests (ARQ) with error correction codes (ECC), have recently demonstrated their potential in enhancing reliability for FSO-based LEO satellite systems [6]–[9]. Notably, the incremental redundancy (IR)-HARQ based on the rate-compatible punctured convolutional code (RCPC) family was studied for the optical satellite systems using rate adaptation [6]. In [7], the authors formulated the power allocation problem of different HARQ variants from the information-theoretic approach for optical satellite systems. The authors addressed the design of a cooperative IR-HARQ for satellite-air-ground integrated networks, incorporating the conventional ARQ and the punctured Reed-Solomon (RS) code [8], [9].

The available studies highlighted the IR-HARQ scheme due to the incremental transmissions of redundancies when the frames are corrupted/uncorrectable. Also, the sliding window mechanism,

in which frames are transmitted continuously without waiting for acknowledgment, is suggested for the IR-HARQ design over long fat networks of FSO-based satellites (long-distance/large bandwidth) [6]. Nevertheless, the existing designs on IR-HARQ in FSO-based satellite systems focused on the ECC using either RS or convolutional punctured codes [10]. As reported in [11], [12], using RS/convolutional codes in FSO systems still demonstrates a considerable gap between their performance and the Shannon limits. This necessitates considering a proper ECC scheme for IR-HARQ designs to further enhance the performance of FSO-based satellite systems.

A feasible and effective solution involves the use of low-density parity check (LDPC) codes for the HARQ designs. The LDPC codes have received tremendous attention thanks to the capacity-approaching performance with low-decoding complexity [13]. It is noteworthy that initial studies on optical satellite systems addressing the design of LDPC codes have been reported in [14]–[16]. Notably, Yamashita et al. composed the LDPC coding scheme to cope with the Markov-based satellite-to-ground optical channel model [14]. In [15], the analysis of non-binary LDPC code and PPM modulation in the optical downlink channel was provided. The authors in [16] investigated the performance of LDPC codes with the interleaved for optical satellite systems.

B. Research Motivation

While the IR-HARQ-based sliding window mechanism/LDPC code is a potential solution, applying such a design for FSO-based satellite systems is challenging and not straightforward for the following reasons. *First*, the existing works on the LDPC design in FSO-based satellite systems [14]–[16] may not be applicable to IR-HARQ design, in which a rate-compatible (RC) structure is required. This structure enables code rate adjustments while utilizing the same encoder/decoder, providing low complexity for IR-HARQ implementation. *Secondly*, the existing IR-HARQ-based LDPC design (process one frame at a time), which has been standardized for RF-based networks (e.g., [17]), is not applicable for long-fat FSO-based satellite networks. FSO operates at exceptionally high data rates (ranging from Gbps to Tbps) with a long turbulence channel coherence time (typically a few milliseconds) [18]. Unlike single-frame transmissions [17], multiple data frames can be accommodated within a coherence time, leading to highly correlated error probabilities of frames, i.e., frame errors tend to happen in bursts. Moreover, the completely different fading models in FSO compared to RF necessitate a proper HARQ design for optimizing system performance [10]. Given the aforementioned reasons, conducting

a comprehensive investigation into the design and performance of IR-HARQ-based RC-LDPC codes in FSO-based LEO satellite systems becomes crucial.

On the other hand, there are two approaches for RC-LDPC code family construction: (i) puncturing and (ii) code extension [19]. The puncturing approach initiates from a low-rate code and progressively removes bits to obtain a higher-rate code. This approach needs painstaking optimization over a large number of punctured patterns and low achievable performance of higher code rates [19]. The latter approach, i.e., code extension, extends and optimizes a parity check matrix of a high-rate code to obtain that of a lower-rate code. This circumvents the critical drawback mentioned in the former approach. It should be noted that the structure of RC-LDPC code families derived by the code extension method can be denoted as the raptor-like structure [20]. Moreover, the code extension method can be effectively conducted on protograph-based LDPC codes, a type of structured LDPC code [19]. The protograph-based LDPC code is also a potential approach for high-speed FSO-based satellite systems thanks to its simple design and hardware-friendly implementation [13]. Capitalizing on the advantages of the code extension method and protograph-based LDPC codes, we consider the joint design of these structures, namely protograph-based raptor-like (PBRL)-LDPC, for the RC-LDPC code in the proposed IR-HARQ scheme.

Aside from our initial reports in [21], [22], to our best knowledge, there have been no other works addressed the design of IR-HARQ with burst transmissions incorporating the PBRL-LDPC in the context of FSO-based LEO satellite systems. The report in [21] conducted a simulation framework to evaluate the goodput and energy efficiency for FSO systems from a satellite to a fixed ground station. The report in [22] provided a mathematical analysis to evaluate the proposed design in terms of goodput. For the sake of simplicity, these studies disregarded critical practical challenges, especially in FSO-based satellite-assisted IoV, such as cloud coverage and transceiver misalignment. Also, another crucial performance metric, i.e., latency, has yet to be explicitly addressed. It is, therefore, imperative to develop a comprehensive analytical framework to gain insight into the performance of FSO-based satellite systems using IR-HARQ with burst transmission/PBRL-LDPC. Crucially, there is a gap in the existing literature regarding the exploration of the feasibility of HARQ implementation in practical FSO systems involving the communication between the LEO satellite and moving vehicles.

TABLE I

LITERATURE ON IR-HARQ AND LDPC OVER FSO-BASED SATELLITE SYSTEMS.

Works	LDPC Design		IR-HARQ	IoV	Practice (e.g., Starlink's data)
	Fixed-rate	Rate-compatible			
[6], [7]	✗	✗	✓	✗	✗
[8], [9]	✗	✗	✓	✓	✗
[14]–[16]	✓	✗	✗	✗	✗
[21], [22]	✓	✓	✓	✗	✗
Our study	✓	✓	✓	✓	✓

C. Major Contributions

This paper offers a complete analytical framework for assessing the performance of FSO-based LEO satellite-assisted IoV using IR-HARQ-based PBRL-LDPC code extension with burst transmissions. Moreover, the paper also aims to explore practical design considerations of IR-HARQ-based PBRL-LDPC over existing SpaceX's Starlink satellite networks. Table I compares our work and the state-of-the-art. In summary, the major contributions of this paper are described as follows.

C_1: *It is the design of IR-HARQ-based RC-LDPC code extension with burst transmission in the context of LEO satellite systems providing high-speed Internet connections for moving vehicles via FSO links.*

Unlike existing studies on HARQ schemes [6]–[9] concentrating on RS/convolutional-based ECC, we consider the PBRL-LDPC, a class of RC-LDPC code extension, for the proposed design. While the use of PBRL-LDPC codes in the design of IR-HARQ is popular, the indispensable novelty of this work is the joint consideration of IR-HARQ-based PBRL-LDPC codes and the burst transmission for high-speed optical satellite systems.

C_2: *We investigate the performance of the proposed system design in practical scenarios involving Starlink's LEO satellites and a moving vehicle in Japan.*

In such scenarios, we consider the real data of Starlink's LEO satellites and the positions of the moving vehicle over the satellite pass duration to compute the zenith angle and the slant path. This allows for an accurate system performance estimation by incorporating all combined effects of the Doppler shift, cloud coverage, atmospheric turbulence, and pointing misalignment.

Additionally, the transceiver misalignment is modeled based on the vibration of the satellite and the sudden change in the vehicle's velocity.

C_3: *We derive a comprehensive analytical framework to assess the performance of the proposed system design in terms of goodput, energy efficiency, and average frame delay.*

It is worth highlighting that modeling and analyzing the performance of IR-HARQ with burst transmission/PBRL-LDPC for such systems is non-trivial. This is because the joint decoding for a frame, which exhibits variations in data size and redundancy, depends on the previously received coded bits experiencing different channel conditions. To tackle this issue, the protograph extrinsic information transfer (PEXIT) algorithm [23] is modified for the considered FSO channel and utilized to obtain the average frame loss rate (FLR). Then, the analysis of the performance metrics is presented based on the derived FLR.

C_4: *From the obtained numerical results, we provide insightful discussions regarding the effectiveness of the design proposal and investigate it under the impact of various channel conditions.*

We perform the Monte Carlo simulations to verify the theoretical model's correctness. Additionally, we highlight the effectiveness of the proposal system by its performance with conventional schemes.

The remainder of this paper is outlined as follows. Section II describes the considered system and FSO channel model. In Section III, we introduce the structure of PBRL-LDPC and illustrate the operation of the IR-HARQ based on the PBRL-LDPC in the considered system. Section IV presents the analytical framework. Numerical results and discussions can be found in Section V. Finally, the paper is concluded in Section VI. For the sake of explicit clarity, the list of abbreviations used in this paper is provided in Table II.

II. SYSTEM AND CHANNEL MODELS

A. System Description

We consider a downlink transmission using FSO from a Starlink's LEO satellite to a self-driving car for IoV applications. For the link-layer's error-control solution, we deploy the IR-HARQ protocol, integrating the sliding window ARQ and the RC-LDPC code extension. The RC-LDPC code detects and corrects erroneous frames using the belief propagation (BP) decoder. If the frames are uncorrected, additional redundancy is retransmitted by the ARQ scheme. This
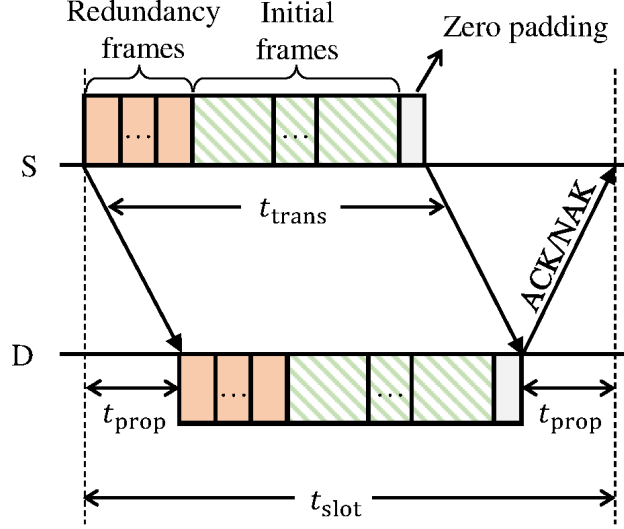
Fig. 1. An illustration of a burst transmission within a time slot.

redundancy is combined with the previously received frames to form a lower-rate coded frame, which increases the chance of successful decoding. The detail of IR-HARQ-based LDPC is described in Section III.

For data transmission, we consider the equal-size time-slot structure. Each time slot contains initial/redundancy frames forming in a burst[1] and the feedback signal (either ACK or NAK), as illustrated in Fig. 1. The feedback channel is assumed to be error-free for ease of analysis. The time-slot duration t_{slot} is given as $t_{\text{slot}} = t_{\text{trans}} + 2t_{\text{prop}}$, where t_{prop} is the propagation delay, and $t_{\text{trans}} = N_{\text{burst}}/R_{\text{b}}$ is the burst transmission delay, with N_{burst} and R_{b} the busrt size and bit rate, respectively. Here, the burst duration should be shorter than the FSO channel coherence time, ensuring consistent channel conditions for frames within bursts.

At the physical layer, we use the on-off keying (OOK) modulation with the intensity modulation/direct detection (IM/DD). Then, the received electrical signal can be computed as [24]

$$y = \Re h x + n, \tag{1}$$

where $\Re$ is the detector responsivity, h is the channel fading coefficient considered to be constant over a burst transmission, $x \in \{x_0 = 0, x_1 = 2P_{\text{t}}\}$ is the transmitted intensity with average

---

[1]It is noted that the initial and redundancy frames may have different sizes, leading to size-varying bursts. To guarantee the same burst duration, zero padding can be appended to a burst together with new/redundancy frames. For such designs, the length of incremental frames cannot exceed that of initial/previous incremental frames. This ensures that a burst transmission can always include all incremental frames from the previous one.

transmitted optical power P_{t}, and $n \sim \mathcal{N}\left(0, \sigma_{\mathrm{n}}^2\right)$ is the additive white Gaussian noise (AWGN). The instantaneous electrical signal-to-noise ratio (SNR) is then expressed as

$$\gamma = \frac{\bar{\gamma} h^2}{\mathbb{E}\left[h^2\right]} = \frac{2\left(\Re P_{\mathrm{t}} h\right)^2}{\sigma_{\mathrm{n}}^2}, \tag{2}$$

where $\bar{\gamma} = \frac{2(\Re P_{\mathrm{t}})^2}{\sigma_{\mathrm{n}}^2} \mathbb{E}\left[h^2\right]$ is the average electrical SNR.

B. Satellite-to-Vehicle FSO Channel Model

This paper considers four major LEO satellite-to-vehicle FSO channel impairments, including the Doppler effect, cloud attenuation, atmospheric turbulence, and pointing error.

1) Doppler Effect: The Doppler frequency shift, denoted by f_{DS}, can be expressed as [25]

$$f_{\mathrm{DS}} = -\frac{R_{\mathrm{E}} R_{\mathrm{S}} \sin\left[\psi_{\mathrm{diff}}(t)\right] \eta\left(\theta_{\max}\right) \omega_F}{\lambda \sqrt{R_{\mathrm{E}}^2 + R_{\mathrm{S}}^2 - 2 R_{\mathrm{E}} R_{\mathrm{S}} \cos\left[\psi_{\mathrm{diff}}(t)\right] \eta\left(\theta_{\max}\right)}}, \tag{3}$$

where $\eta\left(\theta_{\max}\right) = \cos\left[\cos^{-1}\left(\frac{R_{\mathrm{E}}}{R_{\mathrm{S}}} \cos\left(\theta_{\max}\right)\right) - \theta_{\max}\right]$, λ is the optical wavelength, R_{E} is the Earth radius, $R_{\mathrm{S}} = R_{\mathrm{E}} + H_{\mathrm{s}}$ is the satellite orbit radius, H_{s} is satellite's altitude, and $\theta_{\max}$ is the maximum elevation angle. Additionally, $\psi_{\mathrm{diff}}(t)$ is the angular difference between satellite location at time t and its location at maximum elevation angle computed as $\psi_{\mathrm{diff}}(t) \approx \omega_F t$ [25, (10)]. Also, ω_F is the angular velocity of the satellite in the earth-centered fixed (ECF) frame and is approximated as $\omega_F \approx v_{\mathrm{s}}/R_{\mathrm{S}} - \omega_{\mathrm{E}} \cos\left(i_{\mathrm{S}}\right)$, where ω_{E} is the Earth's angular velocity, i_{S} is the satellite's inclination, $v_{\mathrm{s}} = \sqrt{\mu_{\mathrm{G}}/R_{\mathrm{S}}}$ is the satellite's velocity, and $\mu_{\mathrm{G}} = 3.986 \times 10^{14} \mathrm{~m}^3/\mathrm{s}^2$ is the standard gravitational parameter.

Figure 2 illustrates the Doppler frequency shift over a satellite pass duration. Also, different values of the maximum satellite's elevation angle are considered, while $R_{\mathrm{E}} = 6371$ km, $H_{\mathrm{S}} = 500$ km, $\lambda = 1.55~\mu$m, $\omega_{\mathrm{E}} = 72.7~\mu$rad and $i_{\mathrm{S}} = 53°$. From Fig. 2, the value of the Doppler frequency shift is approximately ± 4 GHz. These values are within the current optical receiver design, i.e., ± 14 GHz [26], for which we ignore the Doppler effect in the performance analysis.

2) Cloud Attenuation: Cloud coverage substantially reduces the received optical power due to the scattering effect caused by liquid water particles in clouds. The cloud attenuation, denoted by h_{c}, is calculated as [27]

$$h_{\mathrm{c}} = \exp\left[-\sigma H_{\mathrm{c}} \sec\left(\xi\right)\right], \tag{4}$$
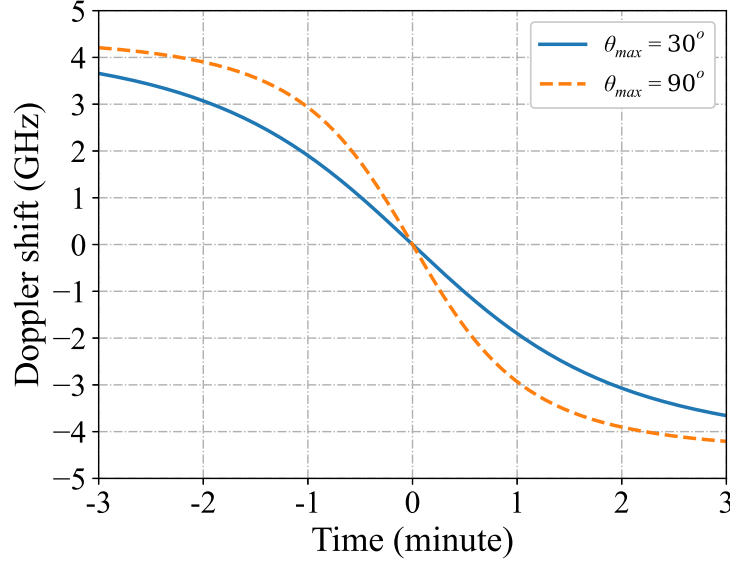
Fig. 2. Doppler frequency shift over the LEO satellite pass duration.

where H_c denotes the vertical extent of clouds, ξ indicates the zenith angle and σ is the attenuation coefficient, which is a function of the visibility V and the optical wavelength λ [18, (4)]. Here, the visibility is written as [28]

$$V = \frac{1.002}{\left(N_c \left[\mathrm{cm}^{-3}\right] \times M_c \left[\mathrm{g/m}^{-3}\right]\right)^{0.6473}}, \tag{5}$$

where M_c is the cloud liquid water content (CLWC), and N_c is the cloud droplet number concentration depending on cloud types, e.g., Nimbostratus N_c = 200 cm^{-3}, Cumulus N_c = 250 cm^{-3}, and Altostratus N_c = 400 cm^{-3} [9].

3) Atmospheric Turbulence: This phenomenon causes scintillation, leading to signal power fluctuations at the receiver's detector. To describe a wide range of turbulence conditions, we consider the Gamma-Gamma distribution, in which the probability density function (PDF) is given as [5]

$$f_{h_t}(h_t) = \frac{2(\alpha\beta)^{\frac{\alpha+\beta}{2}}}{\Gamma(\alpha)\Gamma(\beta)} h_t^{\frac{\alpha+\beta}{2}-1} K_{\alpha-\beta}\left(2\sqrt{\alpha\beta h_t}\right), \tag{6}$$

where $\Gamma(.)$ indicates the Gamma function, $K_{\alpha-\beta}(.)$ denotes the modified Bessel function of the second kind of order $\alpha - \beta$. The large-scale and small-scale turbulence parameters α and

β are written as functions of the Rytov variance σ_{R}^2 [5]. Under the assumption of plane wave propagation, the Rytov variance can be given as [6]

$$\sigma_{\mathrm{R}}^2 = 2.25 k_{\mathrm{wave}}^{7/6} \sec^{11/6}(\xi) \int_{H_{\mathrm{v}}}^{H_{\mathrm{a}}} C_n^2(h)(h - H_{\mathrm{v}})^{5/6} \, \mathrm{d}h, \tag{7}$$

where $k_{\mathrm{wave}} = 2\pi/\lambda$, H_{v} denotes the vehicle's altitude, and H_{a} indicates the atmospheric altitude. Also, $C_n^2(h)$ is modeled by the Hufnagel-Valley model as $C_n^2(h) = 0.00594 \left(\frac{w_{\mathrm{wind}}}{27}\right)^2 (10^{-5}h)^{10}$ $\exp\left(-\frac{h}{1000}\right) + 2.7 \times 10^{-16} \exp\left(-\frac{h}{1500}\right) + C_n^2(0) \exp\left(-\frac{h}{100}\right)$, where $C_n^2(0)$ is the ground-level turbulence, and w_{wind} is rms wind speed [5].

4) Geometric Loss and Misaligment Models: Considering the Gaussian beam profile, the fraction of collected power at the vehicle's detector is approximated as [24]

$$h_{\mathrm{p}} \approx A_0 \exp\left(-\frac{2\rho^2}{w_{L_{\mathrm{eq}}}^2}\right), \tag{8}$$

where ρ is the radial displacement between the centers of the beam footprint and the vehicle detector, $A_0 = [\mathrm{erf}(v)]^2$ is the fraction of the collected power at $\rho = 0$ with $v = (\sqrt{\pi} r_{\mathrm{a}})/(\sqrt{2} w_{L,\mathrm{eff}})$, $\mathrm{erf}(\cdot)$ is the error function, r_{a} is the receiver aperture radius, $w_{L_{\mathrm{eq}}}$ is the equivalent beam width and can be expressed as $w_{L_{\mathrm{eq}}}^2 = w_{L,\mathrm{eff}}^2 \frac{\sqrt{\pi}\,\mathrm{erf}(v)}{2v \exp(-v^2)}$. Also, $w_{L,\mathrm{eff}}$ is the effective beam width in the presence of optical turbulence calculated as $w_{L,\mathrm{eff}} = w_L \sqrt{1 + G_{\mathrm{d}}}$, where G_{d} is in [29, (16)]. Moreover, $w_L = w_0 \sqrt{\left(1 - \frac{L}{F_0}\right)^2 + \left(\frac{2L}{k_{\mathrm{wave}} w_0^2}\right)^2}$, where $w_0 = \frac{\lambda}{\pi\theta}$ and F_0 are, respectively, the satellite's beam radius and radius of curvature, θ is the divergence half-angle.

In addition, as depicted in Fig. 3, the pointing error between the center of the beam footprint and that of the vehicle detector is due to two factors: (1) *the vibration of the satellite* and (2) *the sudden change in the vehicle's velocity that the satellite is not able to keep track of over a short period of time*. In particular, *for the satellite's vibration*, its radial displacement vector is represented as $\boldsymbol{\rho}_{\mathrm{s}} = (a_{\mathrm{x}}, a_{\mathrm{y}})$, where $a_{\mathrm{x}} \sim \mathcal{N}(0, \sigma_{\mathrm{jt}}^2)$ and $a_{\mathrm{y}} \sim \mathcal{N}(0, \sigma_{\mathrm{jt}}^2)$. The variance σ_{jt}^2 is computed based on the jitter angle θ_{jt} and the slant path L as $\sigma_{\mathrm{jt}} \simeq \theta_{\mathrm{jt}} L$. *Regarding the sudden change in the vehicle's velocity*, the radial displacement vector is expressed as $\boldsymbol{\rho}_{\mathrm{v}} = \left(0, \frac{\Delta v \Delta t}{2}\right)$. Here, Δv is the velocity variation over the short time duration Δt, in which $\Delta v \sim \mathcal{N}(0, \sigma_{\mathrm{v}}^2)$. By combining these two factors, the radial displacement vector is expressed as $\boldsymbol{\rho} = (\rho_{\mathrm{x}}, \rho_{\mathrm{y}})$, where $\rho_{\mathrm{x}} \sim \mathcal{N}(0, \sigma_{\mathrm{jt}}^2)$, $\rho_{\mathrm{y}} \sim \mathcal{N}(0, \overline{\sigma}_{\mathrm{v}}^2)$, and $\overline{\sigma}_{\mathrm{v}}^2 = \sigma_{\mathrm{jt}}^2 + \frac{(\Delta t)^2 \sigma_{\mathrm{v}}^2}{4}$. The PDF of $\rho = \|\boldsymbol{\rho}\| = \sqrt{\rho_x^2 + \rho_y^2}$
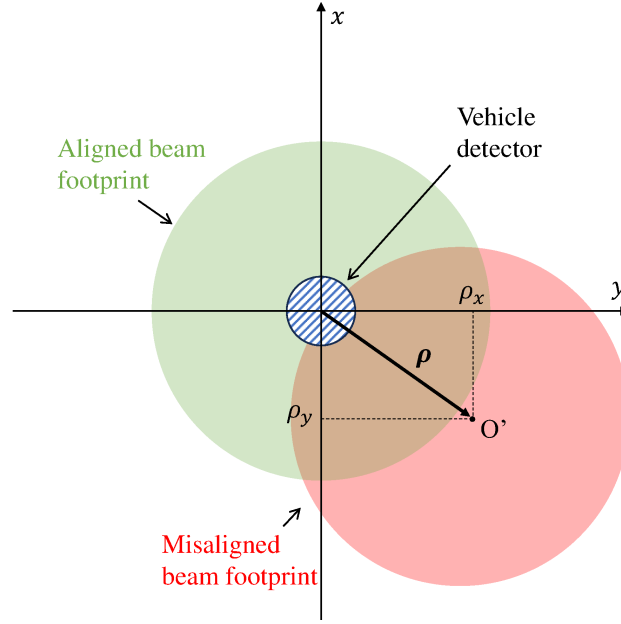
Fig. 3. Misalignment model between LEO satellite and self-driving car.

described by the Hoyt model is given as [30]

$$
\begin{aligned}
f_\rho\left(\rho\right) = \frac{\rho}{\sigma_{\mathrm{jt}}\overline{\sigma}_{\mathrm{v}}} \exp\left[\left(\frac{1}{\sigma_{\mathrm{jt}}^2} + \frac{1}{\overline{\sigma}_{\mathrm{v}}^2}\right)\frac{-\rho^2}{4}\right] \\
\times I_0\left[\left(\frac{1}{\overline{\sigma}_{\mathrm{v}}^2} - \frac{1}{\sigma_{\mathrm{jt}}^2}\right)\frac{\rho^2}{4}\right], \rho > 0,
\end{aligned}
\tag{9}
$$

where $I_0\left(\cdot\right)$ is the modified Bessel function of the first kind.

From (8) and (9), we can obtain the PDF of h_{p}, i.e.,

$$
\begin{aligned}
f_{h_{\mathrm{p}}}\left(h_{\mathrm{p}}\right) = \frac{w_{L_{\mathrm{eq}}}^2}{4h_{\mathrm{p}}\sigma_{\mathrm{jt}}\overline{\sigma}_{\mathrm{v}}}\left(\frac{h_{\mathrm{p}}}{A_0}\right)^{\zeta} \\
\times I_0\left[\left(\frac{1}{\overline{\sigma}_{\mathrm{v}}^2} - \frac{1}{\sigma_{\mathrm{jt}}^2}\right)\left(\frac{-w_{L_{\mathrm{eq}}}^2}{8}\right)\ln\left(\frac{h_{\mathrm{p}}}{A_0}\right)\right],
\end{aligned}
\tag{10}
$$

where $\zeta = \left(\frac{1}{\sigma_{\mathrm{jt}}^2} + \frac{1}{\overline{\sigma}_{\mathrm{v}}^2}\right)\frac{w_{L_{\mathrm{eq}}}^2}{8}$, $0 < h_{\mathrm{p}} \leq A_0$.

$$f_\gamma\left(\gamma\right) = \frac{\pi w_{L_{\mathrm{eq}}}^2}{8\gamma\sigma_{\mathrm{h}}\bar{\sigma}_{\mathrm{h}}\Gamma\left(\alpha\right)\Gamma\left(\beta\right)\sin\left[\pi\left(\alpha-\beta\right)\right]} \sum_{i=0}^{J_{\mathrm{c}}} \frac{1}{i!}\left(\frac{\alpha\beta}{A_0 h_{\mathrm{c}}}\sqrt{\frac{\gamma}{B_0\bar{\gamma}}}\right)^i$$

$$\times\left[\frac{\left(\frac{\alpha\beta}{A_0 h_{\mathrm{c}}}\sqrt{\frac{\gamma}{B_0\bar{\gamma}}}\right)^\beta}{\Gamma\left(i-\alpha+\beta+1\right)\sqrt{\left(i+\beta-\frac{w_{L_{\mathrm{eq}}}^2}{4\bar{\sigma}_{\mathrm{h}}}\right)\left(i+\beta-\frac{w_{L_{\mathrm{eq}}}^2}{4\sigma_{\mathrm{h}}}\right)}}\right.$$

$$\left.-\frac{\left(\frac{\alpha\beta}{A_0 h_{\mathrm{c}}}\sqrt{\frac{\gamma}{B_0\bar{\gamma}}}\right)^\alpha}{\Gamma\left(i+\alpha-\beta+1\right)\sqrt{\left(i+\alpha-\frac{w_{L_{\mathrm{eq}}}^2}{4\bar{\sigma}_{\mathrm{h}}}\right)\left(i+\alpha-\frac{w_{L_{\mathrm{eq}}}^2}{4\sigma_{\mathrm{h}}}\right)}}\right], \tag{12}$$

5) Composite Statistical Channel Model: From (4), (6), and (10), the PDF of the composite channel coefficient $h = h_{\mathrm{c}}h_{\mathrm{t}}h_{\mathrm{p}}$ is given as [30]

$$f_h\left(h\right) = \frac{w_{L_{\mathrm{eq}}}^2\left(\alpha\beta\right)^{\frac{\alpha+\beta}{2}} h^{\zeta-1}}{2\sigma_{\mathrm{jt}}\overline{\sigma}_{\mathrm{v}}\Gamma\left(\alpha\right)\Gamma\left(\beta\right)\left(A_0 h_{\mathrm{c}}\right)^\zeta}$$

$$\times \int_{\frac{h}{A_0 h_{\mathrm{c}}}}^\infty I_0\left[\left(\frac{1}{\overline{\sigma}_{\mathrm{v}}^2}-\frac{1}{\sigma_{\mathrm{jt}}^2}\right)\left(\frac{-w_{L_{\mathrm{eq}}}^2}{8}\right)\ln\left(\frac{h}{A_0 h_{\mathrm{c}}h_{\mathrm{t}}}\right)\right] \tag{11}$$

$$\times h_{\mathrm{t}}^{\frac{\alpha+\beta}{2}-1-\zeta}K_{\alpha-\beta}\left(2\sqrt{\alpha\beta h_{\mathrm{t}}}\right)\mathrm{d}h_{\mathrm{t}}.$$

Using (2), (11), and similar appoach in [31], we can obtain the PDF of γ in (12), where $J_{\mathrm{c}} = \left\lfloor\min\left(\frac{w_{L_{\mathrm{eq}}}^2}{4\sigma_{\mathrm{h}}}, \frac{w_{L_{\mathrm{eq}}}^2}{4\bar{\sigma}_{\mathrm{h}}}\right) - \max\left(\alpha,\beta\right)\right\rfloor$, $\lfloor\cdot\rfloor$ is the floor function.

III. IR-HARQ-BASED RC-LDPC/BURST TRANSMISSIONS

In this section, we address the design of the IR-HARQ protocol, which combines the sliding window ARQ and the protograph-based raptor-like (PBRL)-LDPC code family. First, we present the structure of the RC-LDPC code extension, i.e., the raptor-like structure. Next, the construction of the proposed design based on the protograph is introduced. Finally, we present the operation of the IR-HARQ-based PBRL-LDPC code with burst transmissions for optical satellite systems.

A. Protograph-based Raptor-like LDPC Code

1) RC-LDPC with Raptor-like Structure: To facilitate the operation of the IR-HARQ design, we consider the RC-LDPC code extension, where parity check matric of a low-rate code is
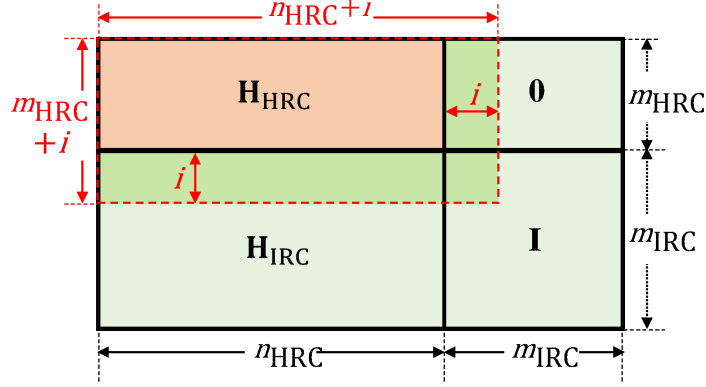
Fig. 4. Structure diagram of the parity check matrix of PBRL-LDPC codes.

obtained by extending that of a higher-rate code. The structure diagram of such RC-LDPC code families is depicted in Fig. 4. Accordingly, the parity check matrix of the lowest code rate is expressed as

$$\mathbf{H} = \left[\begin{array}{cc} \mathbf{H}_{\text{HRC}} & \mathbf{0} \\ \mathbf{H}_{\text{IRC}} & \mathbf{I} \end{array} \right], \tag{13}$$

where $\mathbf{H}_{\text{HRC}}$ is an $m_{\text{HRC}} \times n_{\text{HRC}}$ matrix of the highest-rate codes, $\mathbf{H}_{\text{IRC}}$ is an $m_{\text{IRC}} \times n_{\text{HRC}}$ incremental matrix, $\mathbf{I}$ represents the identity matrix, and $\mathbf{0}$ denotes the all-zero matrix. This type of structure can be denoted as *the raptor-like (RL) structure* [20]. Here, the highest code rate in the family is $\frac{k}{n_{\text{HRC}}}$, where $k = n_{\text{HRC}} - m_{\text{HRC}}$. The matrices of lower-rate codes are derived by extending $\mathbf{H}_{\text{HRC}}$ the same number of rows and columns. Let denote $\mathbf{H}^{(i)}$ as an extended version of $\mathbf{H}_{\text{HRC}}$ by i rows and columns $(0 \leq i \leq n_{\text{IR}})$, which is given as

$$\mathbf{H}^{(i)} = \left[\begin{array}{cc} \mathbf{H}_{\text{HRC}} & \mathbf{0} \\ \mathbf{H}_{\text{IRC}}^{(i)} & \mathbf{I} \end{array} \right], \tag{14}$$

where $\mathbf{H}_{\text{IRC}}^{(i)}$ is the first i rows of $\mathbf{H}_{\text{IRC}}$. The size and code rate of the matrix $\mathbf{H}^{(i)}$ are $(m_{\text{HRC}} + i) \times (n_{\text{HRC}} + i)$ and $\frac{k}{n_{\text{HRC}}+i}$, respectively. These extended matrices have the same information bits k as the base parity check matrix $\mathbf{H}$ but with lower code rates. As a result, we can derive the family of code rates ranging from $\frac{k}{n_{\text{HRC}}}$ to $\frac{k}{n_{\text{HRC}}+n_{\text{IRC}}}$.

Thanks to the raptor-like structure, the encoding of incremental redundancy can be efficiently conducted. The PBRL-LDPC codes can be considered as a concatenated code, where the parity
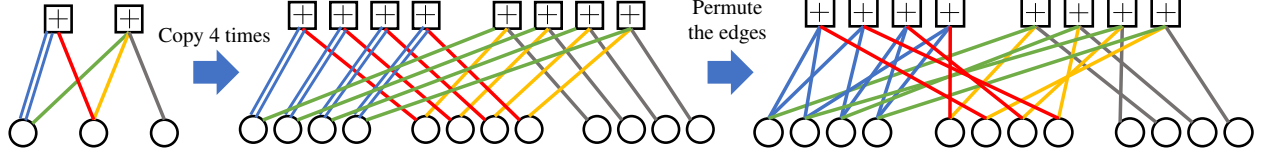
Fig. 5. Copy and permute procedure for a protograph to obtain a lifting graph (circles indicate the variable nodes, and squares represent check nodes).

check matrix of the outer code is $\mathbf{H}_{\text{HRC}}$, and the generator matrix of the inner code is

$$\mathbf{G} = \left[\begin{array}{cc} \mathbf{I} & \mathbf{H}_{\text{IRC}}^{\text{T}} \end{array} \right]. \tag{15}$$

The generator matrix for an arbitrary code rate in the family, for example, $\frac{k}{n_{\text{HRC}}+i}$ $(0 \leq i < n_{\text{IRC}})$, is derived by using i first columns of $\mathbf{G}$. It is apparent that encoded frames with an arbitrary rate are always a part of lower-rate frames. Consequently, we can construct a low-rate frame by adding parity bits to high-rate ones.

2) Protograph-based LDPC Codes: To evaluate the performance of the proposed design, we consider the LDPC code family constructed based on protograph [32]. The key idea of this method was expanding a small matrix, represented by the protograph, into a bigger parity check matrix. In particular, a protograph is a small bipartite graph whose nodes can also be divided into variable nodes (VNs) and check nodes (CNs). A VN can connect to a CN by more than one edge. A protograph can be equivalently represented by a protomatrix $\mathbf{B}$ with the size of $M_{\text{p}} \times N_{\text{p}}$, where M_{p} and N_{p} are the number of CNs and VNs respectively. The code rate of a protograph is computed as $R = \frac{N_{\text{p}} - M_{\text{p}}}{N_{\text{p}}}$. Each element $b_{i,j}$ in the base matrix represented the number of edges connecting the i-th CN to the j-th VN. From a given protograph, a parity check matrix is constructed by duplicating the protograph a number of times q, called the lifting factor. Then, we permute the endpoints of each edge among the same node type. Figure 5 depicts the lifting procedure of a protograph, whose protomatrix is given as

$$\mathbf{B} = \left[\begin{array}{ccc} 2 & 1 & 0 \\ 1 & 1 & 1 \end{array} \right]. \tag{16}$$

Because the derived matrix inherits properties of the protograph, such as the node degree distributions, the analysis of the LDPC code ensemble can be simplified by working on the protograph level [33]. Moreover, the structure of protograph-based LDPC codes can facilitate parallel decoding on hardware, which makes them suitable for high-speed FSO systems [20].

Taking advantage of PB-LDPC codes, the LDPC codes can also be designed from a protograph level. In particular, we start by finding the optimized protomatrix of $\mathbf{H}_{\mathrm{HRC}}$. Then, we gradually extend and optimize each row in the protomatrix of $\mathbf{H}_{\mathrm{HRC}}$. The optimized matrices[2] can be found using the popular exhaustive search [19] or optimization approaches [34]. The objective function in these approaches is often defined as the ensemble decoding threshold of a protograph derived by the PEXIT algorithm.

B. IR-HARQ-based RC-LDPC for Optical Satellite Systems

The operation of IR-HARQ-based PBRL-LDPC code extension is applied to each burst containing multiple frames. On the vehicle-based receiver side, we employ the iterative BP algorithm to decode received frames [35]. Using OOK modulation, the log-likelihood ratio (LLR) of j-th coded bit at the input of the decoder is computed as

$$L_{\mathrm{ch},j} = \log \frac{\Pr(y_j|x_1)}{\Pr(y_j|x_0)} = \frac{2\Re h P_{\mathrm{t}}(y_j - \Re h P_{\mathrm{t}})}{\sigma_{\mathrm{n}}^2}, \tag{17}$$

where h is the instantaneous channel gain considered constant over a burst transmission, modeled by the composite PDF in (12). If the decoding attempt for a frame fails after a determined number of iterations, the frame is marked as erroneous. The information of all erroneous frames in a burst will be contained in the same feedback message sent after the burst transmission. Then, the transmitter sends the redundancies of these erroneous frames in the next burst. Thanks to the raptor-like structure of PBRL-LDPC codes, these redundancies can be appended to already received frames to form lower-rate frames, which increases the chance of successful decoding. The system will discard a frame if its decoding attempts can not be successful after reaching the maximum number of redundancies.

Example 1. *Figure 6 illustrates the IR-HARQ-based RC-LDPC code extension with burst transmission. Also, the RC-LDPC family is $(1, 2/3, 1/2)$. The data frame $F_2^{1^{st}}$ in the first burst is assumed to be corrupted, and the NAK(2) is returned accordingly. In the next burst, the satellite transmits the incremental frame $F_2^{2^{nd}}$, which is combined with $F_2^{1^{st}}$ to form a frame $\left(F_2^{1^{st}}, F_2^{2^{nd}}\right)$ with the code rate of 2/3 for decoding. After the third burst, the combination of $\left(F_2^{1^{st}}, F_2^{2^{nd}}, F_2^{3^{rd}}\right)$ is still uncorrectable. The system then discards these frames as the maximum number of rounds is reached.*

---

[2]The design of optimal LDPC codes for FSO-based satellite turbulence channels is, nevertheless, beyond the scope of this paper.
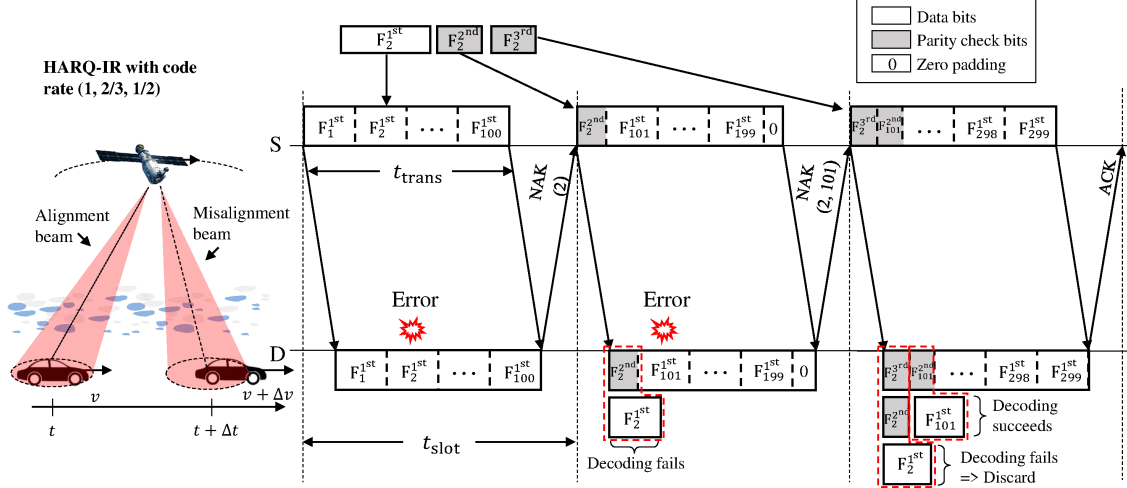
Fig. 6. An example of the IR-HARQ-based RC-LDPC code extension with burst transmission for FSO-based satellite-assisted vehicular systems.

IV. PERFORMANCE ANALYSIS

Utilizing the obtained channel PDF in Section II-B, this section focuses on the performance analysis of the IR-HARQ-based PBRL-LDPC/burst transmission presented in Section III. In particular, we first review the modified PEXIT algorithm, which is used to analyze the decoding-convergence behavior of a PBRL-LDPC code. The average frame loss rate (FLR) is then computed based on this algorithm. Using the derived FLR, we can obtain performance metrics of goodput, energy efficiency, and average frame delay.

A. Modified PEXIT Algorithm

The modified PEXIT algorithm is a mathematical tool to analyze the decoding-convergence behavior of an LDPC code with protograph $\mathcal{G}$ over a channel profile vector $\boldsymbol{\gamma}$ [23], [33]. A protograph $\mathcal{G}$ contains N_{P} variable nodes, M_{P} check nodes, and the corresponding $M_{\mathrm{P}} \times N_{\mathrm{P}}$ protomatrix $\mathbf{B}$. The element $b_{i,j}$ in $\mathbf{B}$ is the number of edges connecting i-th CN to j-th VN. Also, the channel profile vector is $\boldsymbol{\gamma} = (\gamma_1, \gamma_2, \ldots, \gamma_{N_{\mathrm{P}}})$, where γ_j is the SNR experienced by j-th VN. Moreover, we define five types of mutual information (MI) as follows [23]:

- $I_{\mathrm{Av}}(i, j)$: the *a prior* MI received by j-th VN on each of $b_{i,j}$ edges connecting j-th VN and i-th CN.

- $I_{\mathrm{Ac}}(i, j)$: the *a prior* MI received by i-th CN on each of $b_{i,j}$ edges connecting i-th CN and j-th VN.

- $I_{\mathrm{Ev}}(i,j)$: the MI between the message sent by j-th VN to i-th CN and the corresponding coded bit on one of the $b_{i,j}$ edges connecting j-th VN and i-th CN.
- $I_{\mathrm{Ec}}(i,j)$: the MI between the message sent by i-th CN to j-th VN and the corresponding coded bit on one of the $b_{i,j}$ edges connecting i-th CN and j-th VN.
- $I_{\mathrm{app}}(j)$: the a posteriori MI between the posteriori LLR of j-th VN and the corresponding coded bit.

The maximum number of iterations is denoted by $T_{\max}$. In each iteration, we trace the evolution of each aforementioned MI type. As a set of $I_{\mathrm{app}}(j)$ $(1 \leq j \leq N_{\mathrm{p}})$ is yielded at each iteration, the successful convergence is declared if $I_{\mathrm{app}}(j)$, $\forall j$ tend to 1 when the iteration number tends to infinity.

To compute $I_{\mathrm{Ev}}(i,j)$, we consider I_{ch} as the MI between a binary coded bit and its corresponding channel LLR in (17). By assuming all-zero codeword is transmitted, it is observed that $L_{\mathrm{ch}} \sim \mathcal{N}(\sigma_{\mathrm{ch}}^2/2, \sigma_{\mathrm{ch}}^2)$, where $\sigma_{\mathrm{ch}}^2 = \frac{4(\Re h P_{\mathrm{t}})^2}{\sigma_{\mathrm{n}}^2}$. As a result, the considered MI is computed as $J(\sigma_{\mathrm{n}})$, where $J(\cdot)$ is the capacity of the binary-input additive white Gaussian noise channel. Here, $J(\cdot)$ and its inverse function $J^{-1}(\cdot)$ can be found on [36]. Given $i \in \{1, \ldots, M\}$ and $j \in \{1, \ldots, N\}$, the PEXIT algorithm is described as follows:

- **Step 1:** For each j, we initialize $I_{\mathrm{ch}}^{(j)} = J(\sigma_{\mathrm{ch},j})$, where

$$\sigma_{\mathrm{ch},j}^2 = \frac{4(\Re h P_{\mathrm{t}})^2}{\sigma_{\mathrm{n}}^2} = 2\gamma^{(j)}. \tag{18}$$

- **Step 2:** For each (i,j), we compute $I_{\mathrm{Ev}}(i,j)$ using (21) shown in page 18. Then, we set $I_{\mathrm{Ac}}(i,j) = I_{\mathrm{Ev}}(i,j)$. Here, $\Phi(\cdot)$ is the indication function given as

$$\Phi(b_{i,j}) = \begin{cases} 1, & \text{if } b_{i,j} \neq 0, \\ 0, & \text{otherwise.} \end{cases} \tag{19}$$

- **Step 3:** For each (i,j), we compute $I_{\mathrm{Ec}}(i,j)$ using (22) shown in page 18. Then, we set $I_{\mathrm{Av}}(i,j) = I_{\mathrm{Ec}}(i,j)$.

- **Step 4:** For each j, the a posteriori MI is expressed as

$$I_{\mathrm{app}}(j) = J\left(\sqrt{\sum_{s=1}^{M} b_{s,j}\left[J^{-1}(I_{\mathrm{Av}}(s,j))\right]^2 + \sigma_{\mathrm{ch},j}^2}\right). \tag{20}$$

- **Step 5:** Iterate from step 2 to step 4 until $I_{\mathrm{app}}(j) \to 1$, $\forall j$ or the maximum number of iterations $T_{\max}$ is reached.

$$I_{\text{Ev}}(i,j) = \Phi(b_{i,j}) J\left(\sqrt{\sum_{s \neq i} b_{s,j} \left[J^{-1}(I_{\text{Av}}(s,j))\right]^2 + (b_{i,j}-1)\left[J^{-1}(I_{\text{Av}}(i,j))\right]^2 + \left[J^{-1}\left(I_{\text{ch}}^{(j)}\right)\right]^2}\right).$$

(21)

$$I_{\text{Ec}}(i,j) = \Phi(b_{i,j}) \left(1 - J\left(\sqrt{\sum_{s \neq j} b_{i,s}\left[J^{-1}(1 - I_{\text{Ac}}(i,s))\right]^2 + (b_{i,j}-1)\left[J^{-1}(1 - I_{\text{Ac}}(i,j))\right]^2}\right)\right).$$

(22)

Remark 1. *Given the channel profile γ, if $I_{app}(j) \to 1$, $\forall j$ is satisfied, the decoding of LDPC codes based on the protograph $\mathcal{G}$ is successfully conducted with a certain number of iterations.*

B. Average Frame Loss Rate

We now compute the frame loss rate (FLR) of the IR-HARQ scheme. It is defined as the probability that a frame failed after a predefined number of rounds. Let N_{r} and $(C_1 > C_2 > ... > C_{N_{\text{r}}})$ be the HARQ's persistent level and the RC-LDPC family, respectively. Also, $\overline{\text{FLR}}_{n_{\text{r}}}^{(C_1,...,C_{n_{\text{r}}})}$ is the FLR after n_{r}-th round ($n_{\text{r}} \leq N_{\text{r}}$). The FLR for the first transmission with an uncoded frame, $\overline{\text{FLR}}_1^{(1)}$, is calculated as

$$\overline{\text{FLR}}_1^{(1)} = \int_0^\infty f_{1,\gamma}(\gamma)\,\mathrm{d}\gamma$$

$$= \int_0^\infty \left[1 - \left(1 - \overline{\text{BER}}(\gamma)\right)^{N_{\text{d}}}\right] f_\gamma(\gamma)\,\mathrm{d}\gamma,$$

(23)

where $f_\gamma(\cdot)$ is found in (12), N_{d} is the size of the data frame, $\overline{\text{BER}}(\gamma) = Q\left(\sqrt{\frac{\gamma}{2}}\right)$ is the instantaneous bit error rate (BER) with $Q(\cdot)$ the Q-function.

Remark 2. *We can approximate the $\overline{FLR}_1^{(1)}$ using Gauss-Laguerre quadrature method [37, (22.2.13)] as*

$$\overline{FLR}_1^{(1)} \approx \sum_{i=1}^n w_i e^{x_i}\left[1 - \left(1 - \overline{BER}(x_i)\right)^{N_d}\right] f_\gamma(x_i),$$

(24)

where x_i is the i-th root of Laguerre polynomial $L_n(y)$ [37, (25.4.45)], and the weight w_i is given by [37, (25.4.45)]. The approximation (24) quickly converges to the exact form in (23) after $n = 10$ terms.

Next, we determine the FLR of LDPC-coded frames. In fact, the redundancies are transmitted in different time slots, for which LDPC-coded frames may experience different channel SNR values. The channel profile vector is rewritten as $\boldsymbol{\gamma}' = (\gamma_1', \gamma_2', \ldots, \gamma_{N_r}')$, where γ_{n_r}' is the received SNR of coded bits at the n_r-th (re)transmission round. Also, $\overline{\mathbf{D}}_S$ is defined as the outage region of a protograph $\mathcal{G}$. It is a set of $\boldsymbol{\gamma}'$, at which the decoding error probability of LDPC codes cannot be made arbitrarily small, even if the number of decoding iterations is left unbounded [23]. Then, the asymptotic FLR can be computed as [38]

$$
\begin{aligned}
&\overline{\mathrm{FLR}}_{n_r}^{(C_1,\ldots,C_{n_r})} \geq \overline{\mathrm{FLR}}_{n_r,\mathrm{asym}}^{(C_1,\ldots,C_{n_r})} = \\
&\begin{cases}
\displaystyle\int \cdots \int_{\overline{\mathbf{D}}_S} f_{1,\gamma}(\gamma_1')\ldots f_\gamma(\gamma_{n_r}')\,\mathrm{d}\gamma_1'\ldots\mathrm{d}\gamma_{n_r}', & \text{if } C_1 = 1, \\
\displaystyle\int \cdots \int_{\overline{\mathbf{D}}_S} f_\gamma(\gamma_1')\ldots f_\gamma(\gamma_{n_r}')\,\mathrm{d}\gamma_1'\ldots\mathrm{d}\gamma_{n_r}', & \text{if } C_1 \neq 1,
\end{cases}
\end{aligned}
\tag{25}
$$

where $f_\gamma(\cdot)$ and $f_{1,\gamma}(\cdot)$ are found respectively in (12) and (23). To derive the outage region $\overline{\mathbf{D}}_S$, we utilize the exhaustive search method combined with the modified PEXIT algorithm [33]. Furthermore, to clearly illustrate the search process, we provide an example below in cases of $N_r = 2$.

Example 2. *We consider a protograph $\mathcal{G}$ containing M_P CNs and N_P VNs. Also, $N_r = 2$ and the code family of $(1, 1/2)$. There are $N_P/2$ VNs that experience the same SNR of γ_1' while the other $N_P/2$ VNs experience the SNR of γ_2'. The search procedure for the outage zone is described as follows:*

1) *Set the minimum and maximum values of the received SNR to be γ_{min} and γ_{max}, respectively.*
2) *Set the value of γ_1^* to be γ_{min}.*
3) *Exhaustive search for the minimum value of γ_2^* in the range of $[\gamma_{min}, \gamma_{max}]$ so that the iterative decoding can be converged successfully with the channel profile $\boldsymbol{\gamma} = (\gamma_1^*, \gamma_2^*)$. The modified PEXIT algorithm is taken into account in this step. The exhaustive search is effectively conducted utilizing the binary search algorithm.*
4) *Set all the values of (γ_1', γ_2') that qualify $\{(\gamma_1' = \gamma_1^*) \,\&\&\, (\gamma_2' < \gamma_2^*)\}$ to the outage zone.*
5) *Set $\gamma_1^* = \gamma_1^* + 0.1$. If $\gamma_1^* \geq \gamma_{max}$, end the procedure. Otherwise, return to step 3.*
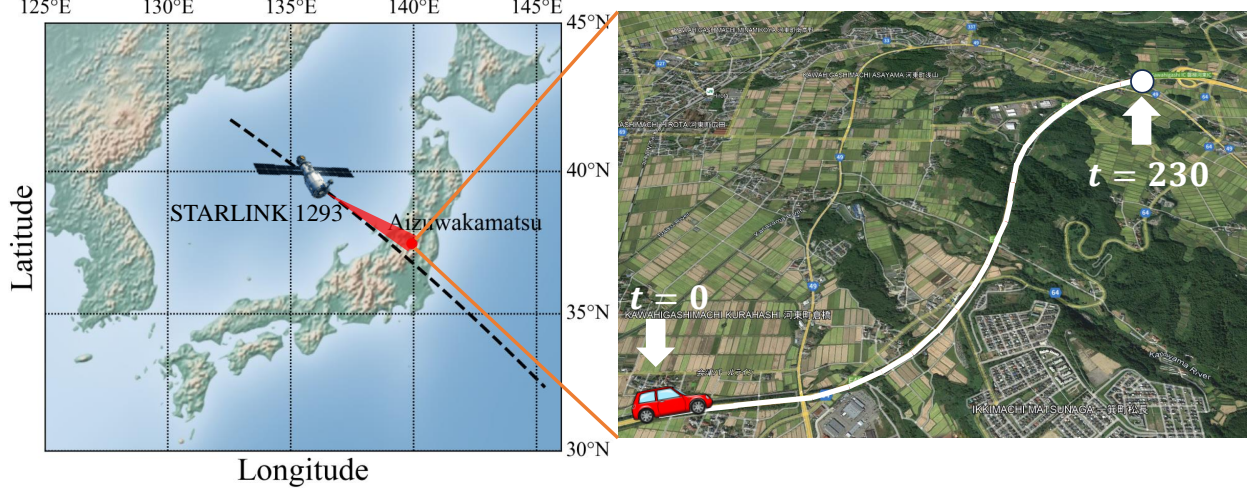
Fig. 7. Illustration of LEO satellite pass over Japan (left side) and the self-driving car moving during the satellite pass duration (right side) on 23 December 2021, 16:09:20:00 UTC+9.

C. Goodput, Energy Efficiency, and Average Frame Delay

Using the FLR derived in Section IV-B, we now calculate the average frame delay, goodput, and energy efficiency.

1) Average Frame Delay: The average frame delay is defined as the number of rounds (in time slots) required for a frame to be transmitted successfully. It is, then, expressed as

$$\overline{D} = \sum_{i=1}^{N_{\mathrm{r}}} i \left(1 - P_{\mathrm{fail}}^{(i)} \right) + N_{\mathrm{r}} P_{\mathrm{fail}}^{(N_{\mathrm{r}})}, \tag{26}$$

where N_{r} is the maximum number of rounds, and $P_{\mathrm{fail}}^{(i)}$ is the probability a the frame is uncorrected at the i-th round, i.e.,

$$P_{\mathrm{fail}}^{(i)} = \begin{cases} \dfrac{\overline{\mathrm{FLR}}_i^{(C_1,\dots,C_i)}}{\overline{\mathrm{FLR}}_{i-1}^{(C_1,\dots,C_{i-1})}}, & \text{if } i \neq 1, \\ \overline{\mathrm{FLR}}_1^{(C_1)}, & \text{if } i = 1, \end{cases} \tag{27}$$

where $\overline{\mathrm{FLR}}_i^{(C_1,\dots,C_i)}$ is found in (25).

2) Goodput Performance: It is defined as the average number of successfully transmitted information bits per second. In particular, the goodput can be computed as

$$\overline{\eta}_{\text{gp}} = \frac{N_{\text{d}} \sum_{i=1}^{N_{\text{r}}} \sum_{j=1}^{i-1} P_{\text{fail}}^{(j)} \left(1 - P_{\text{fail}}^{(i)}\right)}{\sum_{i=1}^{N_{\text{r}}} \sum_{j=1}^{i-1} D_i P_{\text{fail}}^{(j)} \left(1 - P_{\text{fail}}^{(i)}\right)}, \tag{28}$$

where N_{d} is the data frame size, and $P_{\text{fail}}^{(i)}$ is found in (27). In addition, D_i is the average time taken to transmit the frame at the i-th round[3], which can be expressed as

$$D_i = \frac{N_{\text{f}}^{(i)} t_{\text{slot}}}{R_{\text{b}} t_{\text{trans}}}, \tag{29}$$

where R_{b} is the data rate, and $N_{\text{f}}^{(i)}$ is the frame size at the i-th round, which is written as

$$N_{\text{f}}^{(i)} = \begin{cases} N_{\text{d}} \left(\dfrac{1}{C_i} - \dfrac{1}{C_{i-1}} \right), & \text{if } i \neq 1, \\ \dfrac{N_{\text{d}}}{C_1}, & \text{if } i = 1. \end{cases} \tag{30}$$

3) Energy Efficiency: Energy efficiency is defined as the average number of successfully transmitted data bits per joule. Given $\overline{\eta}_{\text{gp}}$ in (28), it is computed as

$$\overline{\eta}_{\text{EE}} = \frac{\overline{\eta}_{\text{gp}}}{P_{\text{t}}}, \tag{31}$$

where P_{t} is the LEO satellite's transmitted power.

V. NUMERICAL RESULTS AND DISCUSSIONS

In this section, we evaluate the performance of the proposed IR-HARQ-based RC-LDPC code extension analyzed in Section IV-C with different parameter settings and practical scenarios. The Monte Carlo simulations are conducted to validate the correctness of theoretical results.

A. Parameter Settings and Practical Scenarios

To construct parity check matrices from protographs, we consider a two-step lifting procedure [40]. The first lifting uses the progressive edge growth (PEG) algorithm to remove all parallel

---

[3]In FSO-based satellite systems, the typical latency values of LDPC frame decoding are in the order of several microseconds [39], which are much smaller than the transmission delay or propagation delay, i.e., a few milliseconds [6]. As a result, we ignore the decoding latency in the goodput performance analysis.

edges. The second lifting uses the circulant PEG algorithm to achieve the quasi-cyclic structure [41]. We utilize the protograph of $\mathbf{H}_{\text{HRC}}$ and $\mathbf{H}_{\text{IRC}}$ in [20, (13, 14)] to construct two sets of RC-LDPC code families, i.e., $(1, 1/2, 1/3)$ and $(1, 2/3, 1/2)$. The first and second lifting factors are 4 and 375, resulting in the information bits $N_{\text{d}} = 12000$. Also, the maximum number of decoding iterations is 100, and the maximum number of rounds N_{r} is 3. The optical beam is supposed to be a collimated Gaussian beam, i.e., $F_0 = \infty$, and the standard deviation of vehicle velocity is 4 m/s. Unless otherwise noted, other system parameters used in this paper are given in Table III.

In addition, the slant distance L and the zenith angle ξ are computed based on the two-line element data sets of satellites and the vehicle's position information [42]. The slant path and zenith angle calculation can be found in the Appendix. For a practical scenario, we use the STARLINK-1293 satellite over Japan, where its two-line element is found in [43]. Also, we start tracking the satellite at $\xi = 60^{\text{o}}$ ($t = 0$). The information related to the receiver's position, i.e., the longitude ϕ_{g}, the latitude λ_{g}, and the elevation h_{g} is extracted from Google Earth Pro shown in Table IV. Here, the starting time $t = 0$ corresponds to 23 December 2021, 16:09:20:00 UTC+9.
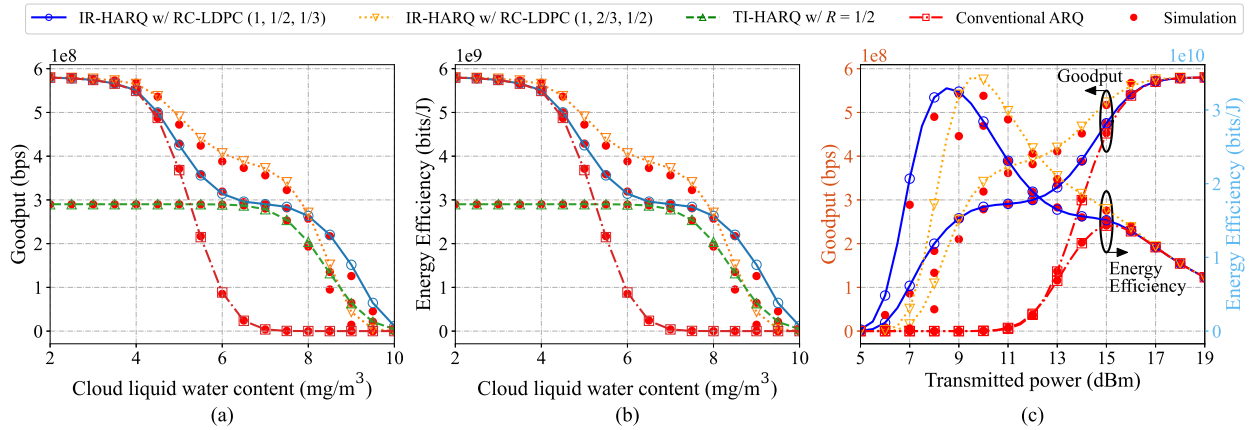
B. Performance Comparison

Fig. 8. (a) Goodput and (b) energy efficiency performance comparison of different link-layer solutions over CLWC, $P_{\text{t}} = 20$ dBm and (c) its tradeoff.

Firstly, we highlight the effectiveness of the proposed IR-HARQ-based RC-LDPC code by comparing its performance with conventional schemes, including (i) type-I (TI) HARQ and (ii)

pure sliding window ARQ. In the TI-HARQ scheme, each burst transmission contains multiple encoded frames with a fixed code rate. If the decoding attempt for a frame fails, the same encoded frame will be retransmitted in the next burst. In addition, the same data frames without ECC will be retransmitted in case of decoding failure for pure sliding window ARQ schemes. A detailed description of these schemes is found in [10].

Figure 8 depicts the performance of our proposed design compared to the TI-HARQ and the sliding window ARQ in terms of goodput and energy efficiency. Also, two different RC-LDPC code families, i.e., $(1, 1/2, 1/3)$ and $(1, 2/3, 1/2)$, are considered. As seen, the theoretical results and simulation ones show a good agreement, confirming the correctness of the analytical framework. Particularly, Figs. 8(a) and (b) investigate the goodput and energy efficiency performance over a range of CLWC values when $P_t = 20$ dBm. As is expected, the performance of the proposed scheme exceeds that of the sliding window ARQ and TI-HARQ for different cloud conditions. This comes from the benefit of retransmitting incremental redundancies for corrupted frames and combining them to correct these frames. It is worth noting that both IR-HARQ and TI-HARQ yield more computational complexity than pure ARQ due to the FEC decoding. Moreover, compared to the TI-HARQ, the proposed IR-HARQ does not increase the system overhead thanks to the RC structure of the LDPC code family. In other words, it allows an encoder/decoder pair to adjust code rates without changing their structure.

In addition, when comparing different RC-LDPC code families, the performance of IR-HARQ using $(1, 2/3, 1/2)$ is better than that of IR-HARQ with $(1, 1/2, 1/3)$ for the CLWC of $M_c < 8 \left(\text{mg/m}^3 \right)$. It is because the incremental retransmissions of the IR-HARQ with $(1, 2/3, 1/2)$ contain fewer parity bits, resulting in more new data frames transmitted in a fixed-duration burst. For example, from Fig. 8(b), when $M_c = 5 \left(\text{mg/m}^3 \right)$, the proposed IR-HARQ-based RC-LDPC using $(1, 2/3, 1/2)$ can achieve the energy efficiency of 5 Gbits/J, while the pure ARQ and TI-HARQ schemes maintain the energy efficiency levels of 4 Gbits/J and 3 Gbits/J, respectively.

We further investigate the trade-off between the goodput and energy efficiency of the proposed design and pure ARQ scheme in Fig. 8(c). Also, different satellite's transmitted powers are taken into account. From the figure, we can select an optimal value of transmitted power to maintain a specific goodput level while maximizing energy efficiency. For example, the optimal values of transmitted power can be selected as 8 dBm, 10 dBm, and 15 dBm to retain the goodput levels of above 200 Mbps, 350 Mbps, and 450 Mbps, for IR-HARQ-based RC-LDPC with $(1, 1/2, 1/3)$, $(1, 2/3, 1/2)$, and pure ARQ scheme, respectively.

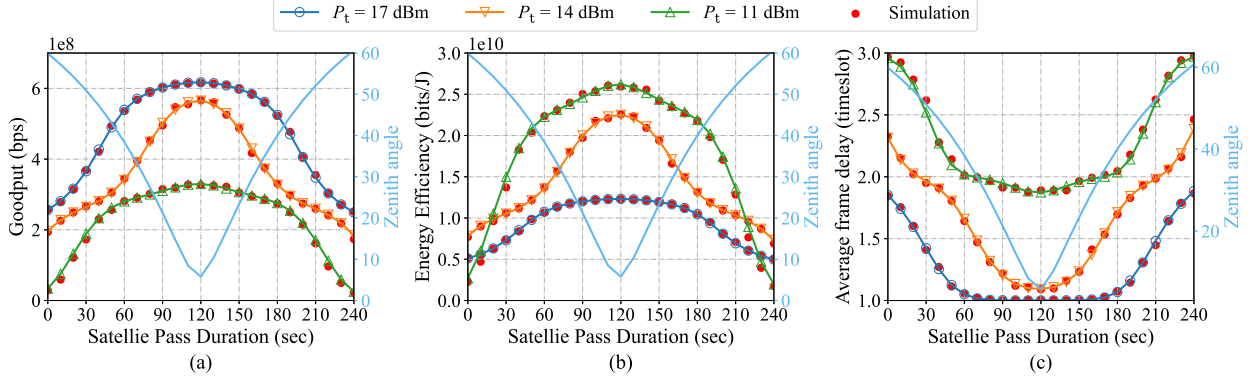## C. Satellite's Transmitted Power Selection

Fig. 9. (a) Goodput, (b) energy efficiency, and (c) average frame delay of the IR-HARQ-based RC-LDPC $(1, 1/2, 1/3)$ over a satellite pass duration for different LEO transmitted powers.

An essential issue for satellite communications is the proper selection of the satellite's transmitted power. For this purpose, we investigate in Fig. 9 the goodput, energy efficiency, and average frame delay of the IR-HARQ-based RC-LDPC $(1, 1/2, 1/3)$ over a satellite pass duration, considering different satellite's transmitted powers. Here, the satellite pass duration is defined as the effective communication time between the LEO satellite and the ground vehicle. The system starts/stops tracking when the zenith angle between satellite and vehicle $\xi = 60°/\xi = -60°$. As is evident, higher values of satellite transmitted power result in higher achievable goodput and lower delay performance. These high values, nonetheless, lead to low energy efficiency. To select the satellite's transmitted power, the rule of thumb is that we need to maintain specific levels of goodput, energy efficiency, and frame delay performance for QoS requirements of applications. For instance, to retain a goodput level of above 200 Mbps, energy efficiency of above 0.8 Gbits/J, and frame delay of 2 timeslots over a satellite pass duration, the transmitted power of LEO satellite should be chosen to be P_t = 14 dBm.

D. Complexity Analysis of Decoding Algorithm

Another important concern for the IR-HARQ-based RC-LDPC design is the complexity of the decoding algorithm, which is indicated by the decoding iteration. Fig. 10 investigates the impact of decoding iteration on the goodput performance of the IR-HARQ-based RC-LDPC $(1, 1/2, 1/3)$ and RC-LDPC $(1, 2/3, 1/2)$. More specifically, Fig. 10(a) and (b) depict the goodput
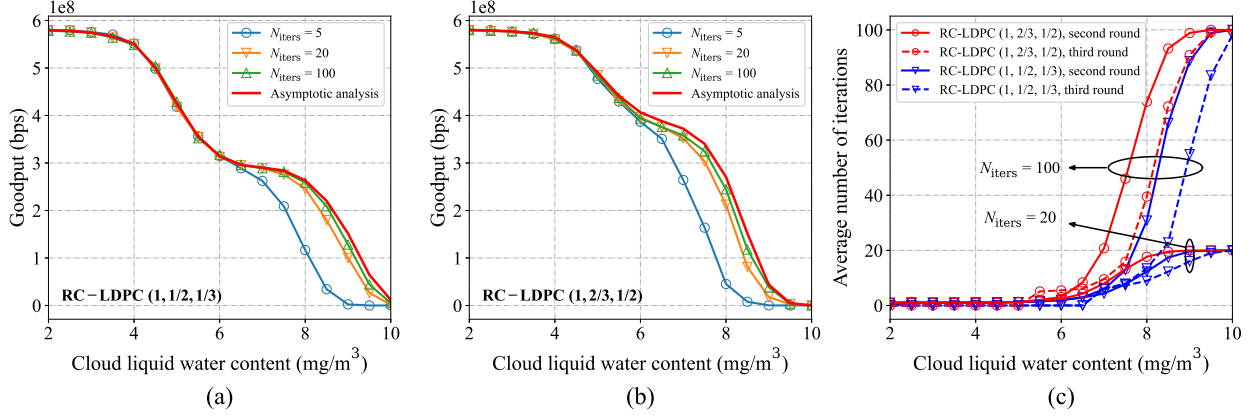
Fig. 10. (a & b) Goodput performance and (c) the average number of iterations of the IR-HARQ-based RC-LDPC over CLWC with different maximum numbers of iterations.

performance of these protocols versus CLWC for different maximum numbers of iterations. Also, the asymptotic analysis achieved by the PEXIT algorithm with a sufficiently large number of iterations is provided. As seen, for the low CLWC values ($M_c < 6$ mg/m^3), we can choose a low number of maximum iterations, e.g., $N_{\text{iters}} = 5$, to reduce the decoding complexity while approaching the asymptotic performance. The impact of the maximum number of iterations becomes clear in the presence of clouds with high CLWC values, e.g., $M_c > 6$ mg/m^3. This is because the BP algorithm needs more iterations to decode a frame successfully for the low-channel SNR values.

Figure 10(c) illustrates the average number of decoding iterations required for a frame at the second and third transmission rounds. Also, two maximum numbers of iterations, i.e., $N_{\text{iters}} = 20$ and $N_{\text{iters}} = 100$, are considered for two different RC-LDPC families, i.e., $(1, 1/2, 1/3)$ and $(1, 2/3, 1/2)$. Obviously, the RC-LDPC $(1, 1/2, 1/3)$ requires fewer iterations to successfully decode a frame compared to RC-LDPC $(1, 2/3, 1/2)$. It is because the lower code rates increase the chance of successfully decoding a frame, resulting in a low achievable average number of iterations. Using this figure, we can also determine N_{iters} to maintain a specific level of goodput performance and the average number of decoding iterations. For example, when $M_c = 8 \left(\text{mg/m}^3\right)$, N_{iters} of the IR-HARQ-based RC-LDPC $(1, 2/3, 1/2)$ can be selected as 20 to maintain a goodput level of 200 Mbps and the average number of decoding iterations below 20.
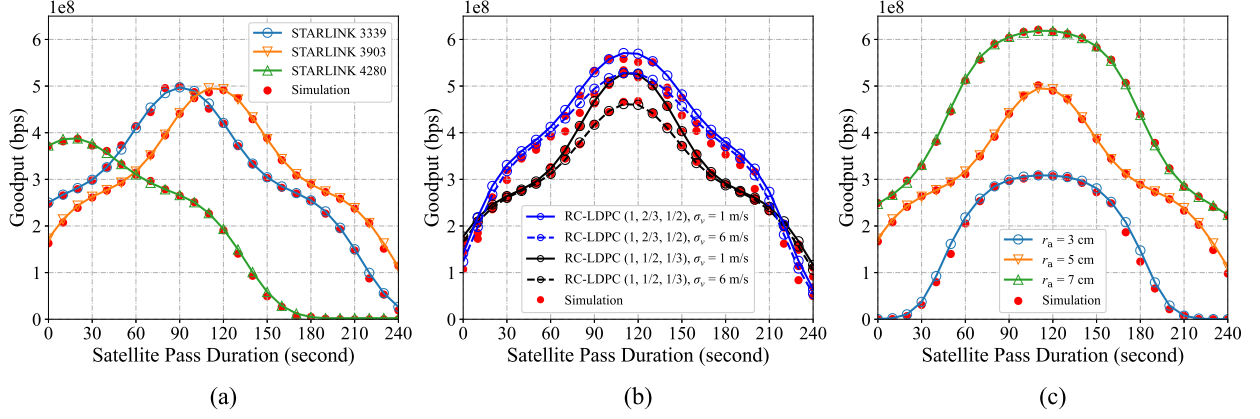
Fig. 11. Goodput performance over a satellite pass duration with different (a) considered satellites; (b) values of velocity variation; (c) values of receiver aperture.

E. Satellite Selection over LEO Constellation

Next, we investigate the satellite selection from the well-known SpaceX's Starlink LEO satellite constellations over Japan. We aim to select a proper LEO satellite to achieve a targeted goodput level while extending the satellite pass duration. Particularly, Fig. 11(a) illustrates the goodput performance of available LEO satellites, i.e., STARLINK 3339, STARLINK 3903, and STARLINK 4280, over the satellite pass duration. Here, we consider a scenario in which a self-driving car starts to select an LEO satellite at time $t = 0$ corresponding to 20 July 2021, 17:42:50 UTC+9. As seen, to maintain a targeted goodput level above 100 Mbps while offering the longest satellite pass duration, it is recommended to choose the STARLINK 3903 satellite.

Using the selected STARLINK 3903 satellite, Fig. 11(b) analyzes the impact of different velocity variation values, i.e., $\sigma_{\rm v} = 1$ m/s and $\sigma_{\rm v} = 6$ m/s, on the goodput performance. Also, two RC-LDPC code families, i.e., $(1, 1/2, 1/3)$ and $(1, 2/3, 1/2)$, are taken into account. As is evident, the impact of pointing errors on the goodput performance is severe during a satellite pass duration. The impact of velocity variation becomes significant for small satellite zenith angles corresponding to narrow beam footprints. From this figure, it is observed that the system using RC-LDPC $(1, 2/3, 1/2)$ offers a higher goodput level than that using the RC-LDPC $(1, 1/2, 1/3)$ over the satellite pass duration. It is because using the RC-LDPC $(1, 2/3, 1/2)$ is enough for error correction under the impact of pointing misalignment. At the same time, using stronger family codes with more redundancies may lead to reduced goodput performance.

Finally, we analyze the goodput performance during a satellite pass duration over a range of

$$\mathbf{R} = \begin{pmatrix} \cos\omega\cos\Omega - \sin\omega\cos i\sin\Omega & -\sin\omega\cos\Omega - \cos\omega\cos i\sin\Omega & \sin\Omega\sin i \\ \cos\omega\sin\Omega + \sin\omega\cos i\cos\Omega & -\sin\omega\sin\Omega + \cos\omega\cos i\cos\Omega & -\cos\Omega\sin i \\ \sin\omega\sin i & \cos\omega\sin i & \cos i \end{pmatrix}. \tag{32}$$

receiver aperture radius values in Fig. 11(c). Also, the RC-LDPC $(1, 1/2, 1/3)$ is considered. Clearly, the goodput performance is enhanced for a larger receiver aperture size. Using this figure, we can determine the receiver aperture size to maintain a targeted level of goodput performance. For instance, the receiver aperture radius should be selected as 7 cm to retain a targeted goodput performance of above 200 Mbps during the satellite pass duration.

VI. CONCLUSION

This paper has addressed the design of the IR-HARQ-based RC-LDPC code extension for the FSO-based LEO satellite systems. A comprehensive analytical framework based on the PEXIT algorithm was provided to evaluate the performance of the design proposal in terms of goodput, energy efficiency, and average frame delay. Moreover, we considered the real data of STARLINK's LEO satellites and the moving vehicle to accurately estimate the system's performance. Monte Carlo simulations were conducted to verify the correctness of the mathematical framework. From the numerical results, we highlighted the effectiveness of the proposed design compared to other link-layer solutions, i.e., the TI-HARQ and the conventional pure ARQ schemes. In addition, insightful discussions regarding the proper selection of transmitted power and decoding complexity concerns were provided. Finally, we discussed the selection of LEO satellites and system parameters in the considered scenario.

APPENDIX A
CALCULATION OF SLANT PATH AND ZENITH ANGLE

This section calculates the slant path L and zenith angle ξ between a satellite and a ground receiver given the two-line element set of a satellite. First, we compute the coordinate of the
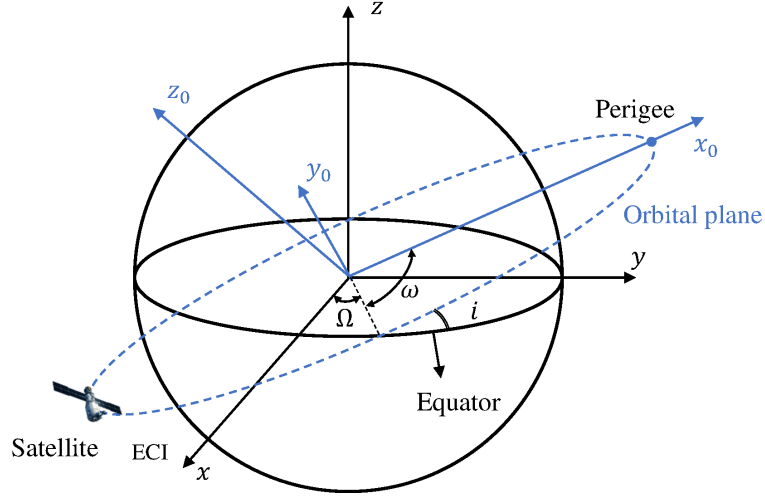
Fig. 12. Orbital plane coordinates (x_0, y_0, z_0) and earth-centered inertial (ECI) coordinates (x, y, z).
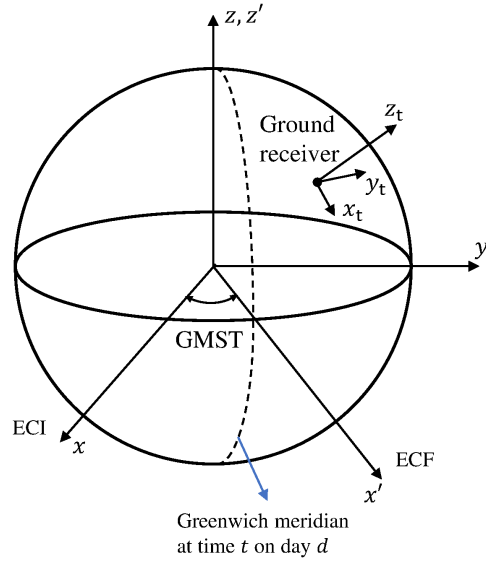

Fig. 13. ECI coordinates (x, y, z), earth-centered fixed (ECF) coordinates (x', y', z'), and topocentric coordinate (x_t, y_t, z_t).

satellite in its orbital coordinate system (x_0, y_0, z_0) as

$$\begin{cases} x_0 = a \left(\cos E - e \right) \\ y_0 = a \sqrt{1 - e^2} \sin E \ , \\ z_0 = 0 \end{cases} \tag{33}$$

where a is the length of the orbit's semi-major axis, and e is the orbital eccentricity. Additionally, E is the eccentric anomaly computed as a function of the mean anomaly M, i.e., $E \approx M + e \sin M + \frac{e^2}{2} \sim 2M + \frac{e^3}{8} \left(3 \sin 3M - \sin M\right)$. Moreover, a is expressed as $a = \sqrt[3]{\frac{n^2}{\mu}}$, where n is the mean motion, and μ_{G} is the standard gravitational parameter. Next, we transform the coordinate of the system to the earth-centered inertial (ECI) coordinate system as shown in Fig. 12, i.e.,

$$
\begin{pmatrix} x \\ y \\ z \end{pmatrix} = \mathbf{R} \begin{pmatrix} x_0 \\ y_0 \\ z_0 \end{pmatrix}, \tag{34}
$$

where $\mathbf{R}$ is the rotation matrix found in (32). Therein, ω is the argument of perigee, Ω is the right ascension of the ascending node, and i_{S} is the inclination. In the next step, we change the coordinate of the satellite in the ECI to the earth-centered fixed (ECF) coordinate system as depicted in Fig. 13, and find the coordinate of the ground receiver. For the coordinate of the satellite, its ECF coordinate is computed as

$$
\begin{cases} x' = x \cos \mathrm{GMST} + y \sin \mathrm{GMST} \\ y' = -x \sin \mathrm{GMST} + y \cos \mathrm{GMST}\,, \\ z' = z \end{cases} \tag{35}
$$

where GMST is the Greenwich mean sidereal time in degree at time t on day d of the observed year and can be computed using [42, (3-49)]. On the other hand, the coordination of the ground receiver in the ECF coordinate system is

$$
\begin{cases} x'_{\mathrm{g}} = (R_{\mathrm{E}} + h_{\mathrm{g}}) \cos \phi_{\mathrm{g}} \cos \lambda_{\mathrm{g}} \\ y'_{\mathrm{g}} = (R_{\mathrm{E}} + h_{\mathrm{g}}) \cos \phi_{\mathrm{g}} \sin \lambda_{\mathrm{g}}\,, \\ z'_{\mathrm{g}} = (R_{\mathrm{E}} + h_{\mathrm{g}}) \sin \phi_{\mathrm{g}} \end{cases} \tag{36}
$$

where R_{E} is the Earth radius, ϕ_{g} is the longitude of the ground receiver, λ_{g} is the latitude of the ground receiver, h_{g} is the elevation at the location of the ground receiver. Then we transform the ground station-satellite vector in the ECF coordinate system to the topocentric coordinate system as follows

$$
\begin{pmatrix} x_{\mathrm{t}} \\ y_{\mathrm{t}} \\ z_{\mathrm{t}} \end{pmatrix} = \mathbf{A} \begin{pmatrix} x' - x'_{\mathrm{g}} \\ y' - y'_{\mathrm{g}} \\ z' - z'_{\mathrm{g}} \end{pmatrix}, \tag{37}
$$

where $\mathbf{A}$ is the rotation matrix in the form of

$$\mathbf{A} = \begin{pmatrix} \sin\phi_{\mathrm{g}}\cos\lambda_{\mathrm{g}} & \sin\phi_{\mathrm{g}}\sin\lambda_{\mathrm{g}} & -\cos\phi_{\mathrm{g}} \\ -\sin\lambda_{\mathrm{g}} & \cos\lambda_{\mathrm{g}} & 0 \\ \cos\phi_{\mathrm{g}}\cos\lambda_{\mathrm{g}} & \cos\phi_{\mathrm{g}}\sin\lambda_{\mathrm{g}} & \sin\phi_{\mathrm{g}} \end{pmatrix}. \tag{38}$$

Based on (37), the slant path L and the zenith angle ξ can be computed as

$$L = \sqrt{x_{\mathrm{t}}^2 + y_{\mathrm{t}}^2 + z_{\mathrm{t}}^2}, \quad \xi = 90^o - \arctan\left(\frac{z_{\mathrm{t}}}{\sqrt{x_{\mathrm{t}}^2 + y_{\mathrm{t}}^2}}\right). \tag{39}$$

REFERENCES

[1] B. Ji *et al.*, "Survey on the internet of vehicles: Network architectures and applications," *IEEE Commun. Standards Mag.*, vol. 4, no. 1, pp. 34–41, Mar. 2020.

[2] N. Saeed, H. Almorad, H. Dahrouj, T. Y. Al-Naffouri, J. S. Shamma, and M.-S. Alouini, "Point-to-point communication in integrated satellite-aerial 6G networks: State-of-the-art and future challenges," *IEEE Open J. Commun. Soc.*, vol. 2, pp. 1505–1525, Jun. 2021.

[3] M. A. Khalighi and M. Uysal, "Survey on free space optical communication: A communication theory perspective," *IEEE Commun. Surv. Tutor.*, vol. 16, no. 4, pp. 2231–2258, Jun. 2014.

[4] S. Wang *et al.*, "Performance analysis of satellite-vehicle networks with a non-terrestrial vehicle," *IEEE Trans. Intell. Veh.*, early access, doi: 10.1109/JPROC.2010.2070470.

[5] J. Ma, K. Li, L. Tan, S. Yu, and Y. Cao, "Performance analysis of satellite-to-ground downlink coherent optical communications with spatial diversity over gamma–gamma atmospheric turbulence," *Appl. Opt.*, vol. 54, no. 25, pp. 7575–7585, Aug. 2015.

[6] H. D. Le and A. T. Pham, "On the design of FSO-based satellite systems using incremental redundancy hybrid ARQ protocols with rate adaptation," *IEEE Trans. Veh.*, vol. 71, no. 1, pp. 463–477, Nov. 2021.

[7] T. T. Kapsis and A. D. Panagopoulos, "Power allocation for reliable and energy-efficient optical LEO-to-ground downlinks with hybrid ARQ schemes," *MDPI Photonics*, vol. 9, no. 2, p. 92, Feb. 2022.

[8] H. D. Nguyen, H. D. Le, C. T. Nguyen, and A. T. Pham, "Throughput and delay performance of cooperative HARQ in satellite-HAP-vehicle FSO systems," in *Proc. IEEE Veh. Technol. Conf*, Sept. 2021, pp. 1–6.

[9] H. D. Le, H. D. Nguyen, C. T. Nguyen, and A. T. Pham, "FSO-based space-air-ground integrated vehicular networks: Cooperative HARQ with rate adaptation," *IEEE Trans. Aerosp. Electron. Syst.*, Jan. 2023, doi: 10.1109/TAES.2023.3236904.

[10] H. D. Le and A. T. Pham, "Link-layer retransmission-based error-control protocols in FSO communications: A survey," *IEEE Commun. Surv. Tuts*, vol. 24, no. 3, pp. 1602–1633, Thirdquarter 2022.

[11] J. Anguita, I. Djordjevic, M. Neifeld, and B. Vasic, "Shannon capacities and error-correction codes for optical atmospheric turbulent channels," *J. Opt. Commun. Netw.*, vol. 4, no. 9, pp. 586–601, Sept. 2005.

[12] W. Gappmair and M. Flohberger, "Error performance of coded FSO links in turbulent atmosphere modeled by gamma-gamma distributions," *IEEE Trans. Wireless Commun.*, vol. 8, no. 5, pp. 2209–2213, May 2009.

[13] Y. Fang, G. Bi, Y. L. Guan, and F. C. Lau, "A survey on protograph LDPC codes and their applications," *IEEE Commun. Surv. Tutor.*, vol. 17, no. 4, pp. 1989–2016, Fourthquarter 2015.

[14] Y. Yamashita, E. Okamoto, Y. Iwanami, Y. Shoji, M. Toyoshima, and Y. Takayama, "A markov-based satellite-to-ground optical channel model and its effective coding scheme," *IEICE Trans. Commun.*, vol. 95, no. 1, pp. 254–262, Jan. 2012.

[15] J. Liu *et al.*, "A novel multi-LDPC-NPPM modulation coding scheme for satellite ground laser communications," in *Proc. Int. Conf. Opt. Commun. Netw. (ICOCN)*, 2016, pp. 1–3.

[16] D. T. Nguyen and Y. Park, "Performance analysis of interleaved LDPC for optical satellite communications," *Opt. Commun.*, vol. 442, pp. 13–18, 2019.

[17] "Multiplexing and channel coding (release 15)," 3GPP, document TS 38.212 V15.1.1, Apr. 2018.

[18] H. D. Le and A. T. Pham, "Level crossing rate and average fade duration of satellite-to-UAV FSO channels," *IEEE Photon. J.*, vol. 13, no. 1, pp. 1–14, Feb. 2021.

[19] T. Van Nguyen, A. Nosratinia, and D. Divsalar, "The design of rate-compatible protograph LDPC codes," *IEEE Trans. Commun.*, vol. 60, no. 10, pp. 2841–2850, Aug. 2012.

[20] T.-Y. Chen, K. Vakilinia, D. Divsalar, and R. D. Wesel, "Protograph-based raptor-like LDPC codes," *IEEE Trans. Commun.*, vol. 63, no. 5, pp. 1522–1532, Feb. 2015.

[21] C. T. Nguyen, H. D. Le, and A. T. Pham, "Performance of IR-HARQ-based RC-LDPC code extension in optical satellite systems," in *Proc. IEEE VTS Asia–Pacific Wireless Commun. Symp. (APWCS)*, Aug. 2023, pp. 1–6.

[22] ——, "Goodput performance of LDPC-based HARQ protocol in FSO-based vertical systems," *IEICE Proc. Ser.*, vol. 79, no. P1-9, 2023.

[23] P. Pulini, G. Liva, and M. Chiani, "Unequal diversity LDPC codes for relay channels," *IEEE Trans. Wireless Commun.*, vol. 12, no. 11, pp. 5646–5655, Nov. 2013.

[24] A. A. Farid and S. Hranilovic, "Outage capacity optimization for free-space optical links with pointing errors," *IEEE/OSA J. Lightwave Technol.*, vol. 25, no. 7, pp. 1702–1710, July 2007.

[25] I. Ali, N. Al-Dhahir, and J. E. Hershey, "Doppler characterization for LEO satellites," *IEEE Trans. Commun.*, vol. 46, no. 3, pp. 309–313, Mar. 1998.

[26] J. Li, Y. Yao, G. Wu, J. Hou, W. Yu, B. Liu, and J. Liu, "Broadband laser doppler frequency shift emulator for satellite laser communication," *IEEE Photon. J.*, vol. 11, no. 6, pp. 1–12, Dec. 2019.

[27] Z. Ghassemlooy, W. Popoola, and S. Rajbhandari, *Optical wireless communications: system and channel modelling with MATLAB®*, 1st ed.   Boca Raton, FL, USA: CRC press, 2019.

[28] H. D. Le, T. V. Nguyen, and A. T. Pham, "Cloud attenuation statistical model for satellite-based FSO communications," *IEEE Antennas Wireless Propag. Lett.*, vol. 20, no. 5, pp. 643–647, May 2021.

[29] L. Andrews, R. Phillips, and P. Yu, "Optical scintillations and fade statistics for a satellite-communication system," *OSA Appl. Opt.*, vol. 34, no. 33, pp. 7742–7751, Nov. 1995.

[30] M. Q. Vu, T. V. Pham, N. T. Dang, and A. T. Pham, "Design and performance of relay-assisted satellite free-space optical quantum key distribution systems," *IEEE Access*, vol. 8, pp. 122 498–122 510, 2020.

[31] K.-J. Jung, S. S. Nam, M.-S. Alouini, and Y.-C. Ko, "Unified finite series approximation of FSO performance over strong turbulence combined with various pointing error conditions," *IEEE Trans. Commun.*, vol. 68, no. 10, pp. 6413–6425, Oct. 2020.

[32] J. Thorpe, "Low-density parity-check (LDPC) codes constructed from protographs," *Proc. IPN Progr. Rep.*, vol. 42, no. 154, pp. 42–154, Aug. 2003.

[33] Y. Fang, G. Bi, and Y. L. Guan, "Design and analysis of root-protograph LDPC codes for non-ergodic block-fading channels," *IEEE Trans. Wireless Commun.*, vol. 14, no. 2, pp. 738–749, Feb. 2015 .

[34] H. Uchikawa, "Design of non-precoded protograph-based LDPC codes," in *Proc. IEEE Int. Symp. Inf. Theory*, Jun. 2014, pp. 2779–2783 .

[35] T. J. Richardson and R. L. Urbanke, "The capacity of low-density parity-check codes under message-passing decoding," *IEEE Trans. Inf. Theory*, vol. 47, no. 2, pp. 599–618, Feb. 2001.

[36] S. Ten Brink, G. Kramer, and A. Ashikhmin, "Design of low-density parity-check codes for modulation and detection," *IEEE Trans. Commun.*, vol. 52, no. 4, pp. 670–678, Apr. 2004.

[37] M. Abramowitz and I. A. Stegun, *Handbook of Mathematical Functions: With Formulas, Graphs, and Mathematical Tables*, 1st ed. New York, NY, USA: Dover, 1972.

[38] C. Kim, S.-H. Kim, and J.-S. No, "New GRP LDPC codes for H-ARQ-IR over the block fading channel," *IEEE Trans. Commun.*, vol. 68, no. 11, pp. 6642–6656, Nov. 2020 .

[39] A. Naderi, S. Mannor, M. Sawan, and W. J. Gross, "Delayed stochastic decoding of LDPC codes," *IEEE Trans. Signal Process.*, vol. 59, no. 11, pp. 5617–5626, 2011 .

[40] D. G. Mitchell, R. Smarandache, and D. J. Costello, "Quasi-cyclic LDPC codes based on pre-lifted protographs," *IEEE Trans. Inf. Theory*, vol. 60, no. 10, pp. 5856–5874, 2014.

[41] Z. Li and B. V. Kumar, "A class of good quasi-cyclic low-density parity check codes based on progressive edge growth graph," in *Proc. 38th Asilomar Conf. Signals. Syst. Comput.*, vol. 2, 2004, pp. 1990–1994.

[42] W. L. Pritchard, H. G. Suyderhoud, and R. A. Nelson, *Satellite Communications Systems Engineering*, 2nd ed. Pearson Education India, 1993.

[43] "CelesTrak". Accessed: Jan. 16, 2024. [Online]. Available: https://celestrak.org/

TABLE II

LIST OF ABBREVIATIONS

Acronyms	Description
ACK	Acknowledgment
ARQ	Automatic Repeat Request
BER	Bit-Error Rate
BP	Belief Propagation
CLWC	Cloud Liquid Water Content
CN	Check Node
ECC	Error Correction Code
ECI	Earth-Centered Inertial
ECF	Earth-Centered Fixed
FLR	Frame Loss Rate
FSO	Free-Space Optical
GMST	Greenwich Mean Sidereal Time
HARQ	Hybrid Automatic Repeat Request
IM/DD	Intensity Modulation/Direct Detection
IoV	Internet of Vehicles
LDPC	Low-Density Parity Check Code
LEO	Low-Earth Orbit
LLR	Log-Likelihood Ratio
MI	Mutual Information
NAK	Negative acknowledgment
OOK	On-Off Keying
PBRL	Protograph-Based Raptor-Like
PDF	Probability Density Function
PEXIT	Protograph Extrinsic Information Transfer Chart
RC	Rate-Compatible
RCPC	Rate-Compatible Punctured Convolutional
RS	Reed-Solomon
SNR	Signal-to-Noise Ratio
TI-HARQ	Type I-Hybrid Automatic Repeat Request
VN	Variable Node

TABLE III

SYSTEM PARAMETERS

Name	Symbol	Value
LEO Satellite (Transmitter)		
Divergence half-angle	θ	20 μrad
Bit rate	R_{b}	1 Gbps
Burst duration	t_{burst}	6 ms
Optical wavelength	λ	1550 nm
Jitter angle	θ_{jt}	2 μrad
Vehicle (Receiver)		
Vehicle altitude	H_{v}	1.5 m
Aperture radius	r_{a}	5 cm
Noise standard deviation	σ_{n}	10^{-7} A/Hz
Detector responsivity	$\mathfrak{R}$	0.9
Other Parameters		
Atmospheric altitude	H_{a}	20 km
Rms wind speed	w_{wind}	21 m/s
Ground turbulence level	$C_n^2(0)$	10^{-14} m$^{-2/3}$
Vertical extent of cloud	H_{c}	2 km
Cloud liquid water content	M_{c}	1 mg/m^3
Cloud droplet number concentration	N_{c}	250 cm^{-3}

TABLE IV

Positions of vehicles over the STARLINK-1293's pass duration on 23 December 2021, 16:09:20:00 UTC+9

Time (s)	Latitude λ_g	Longitude ϕ_g	Elevation h_g (m)
0	37.527626810	139.937772399	202.1
10	37.527918445	139.939627360	209.2
20	37.528057200	139.941509785	214.4
30	37.528223259	139.943385492	218.5
40	37.528434958	139.945259299	227.0
50	37.528919317	139.947038189	232.1
60	37.529639038	139.948700980	241.5
70	37.530531258	139.950219235	251.0
80	37.531639611	139.951508478	250.8
90	37.532863448	139.952606684	259.0
100	37.534143150	139.953605966	263.2
110	37.535497196	139.954427033	262.6
120	37.536893911	139.955117590	265.4
130	37.538313844	139.955737223	289.5
140	37.539797337	139.956140339	282.0
150	37.541268436	139.956446573	296.7
160	37.542742320	139.956837665	288.4
170	37.544143595	139.957526339	288.1
180	37.545433175	139.958499501	304.6
190	37.546628063	139.959641783	315.1
200	37.547731262	139.960928579	320.6
210	37.548754209	139.962311676	306.6
220	37.549618044	139.963862908	322.9
230	37.550289206	139.965555254	330.1
240	37.550796657	139.967336949	340.6